Highly efficient photocatalyst based on all oxides WO$_3$/Cu$_2$O heterojunction for photoelectrochemical water splitting

Jing Zhang [a], Haipeng Ma [b], Zhifeng Liu [a,*]

[a] School of Materials Science and Engineering, Tianjin Chengjian University, 300384, Tianjin, China
[b] School of Civil Engineering and Achitecture, Xinxiang University, Xinxiang, 453003, China

A B S T R A C T

We present a novel all oxides semiconductor WO$_3$/Cu$_2$O heterojunction photoelectrode applied in photoelectrochemical water splitting. Different amount of Cu$_2$O was loaded onto WO$_3$ NRs by controlling the electrodeposition time and the amount influence on the photoelectrocatalytic activity of the different samples has been researched. This all oxides structure exhibits a remarkably high photoelectrocatalytic performance with a significant improved photocurrent density of 1.37 mA cm^{-2} was measured at a bias voltage of 0.8 V vs RHE, which was about 3.51 times higher than that of pristine WO$_3$ NRs. This amazing PEC performance due to the broader light absorption spectrum, the enhanced photogenerated charge carriers transfer efficiency and the suppressive electron-hole recombination rate. The research results can demonstrate a promising way for designing all oxide semiconductor heterojunction structure so that it can improve photoelectrocatalytic efficiency. Moreover, these results also suggest that the WO$_3$ NRs/Cu$_2$O arrays heterojunction structure has a great potential application for efficient PEC water splitting devices.

© 2016 Elsevier B.V. All rights reserved.

1. Introduction

In sustainable-energy societies, the exploitation of renewable energy sources becomes urgent to alleviate the effects of increasing energy requirement. In fact, hydrogen has been considered as a clean and storable energy carrier which produced from renewable solar energy could mitigate many energy and environmental issues [1,2]. Photoelectrochemical (PEC) water splitting based on semiconductors for hydrogen generation driven by sunlight irradiation continues to attract worldwide interest as a highly-efficient, eco-friendly and promising technique when Fujishima and Honda firstly reported the photoelectrochemical water splitting using a TiO$_2$ electrode in 1972 [3]. Owing to the PEC water splitting process is grounded on the photoactivation of semiconductor electrodes, fundamental and applied research for overcoming the efficiency and durability barriers in semiconductor materials are essential. Various metal oxides semiconductors have been utilized in PEC water splitting as an electrode, including TiO$_2$ [4], ZnO [5], Fe$_2$O$_3$ [6], BiVO$_4$ [7] and WO$_3$ [8]. In particular, WO$_3$ is widely applied in high-efficiency PEC water splitting, due to its resilience to photocorrosion effect in aqueous solution,

visible-light-harvesting properties and efficient electron transport properties [9,10]. Recently, Wang et al. have fabricated hexagonal phase WO$_3$ nanoflower as high-quanlity photoelectrode used in PEC water splitting and showed the incident photon-to-current efficiency of ∼29% [11].

Whereas, WO$_3$ nanomaterials still suffer from their sluggish transfer of charge at the semiconductor/electrolyte interface and high electron-hole recombination rate. Vast quantities of efforts have been focused on overcoming the issues above and improving the photoelectrocatalytic properties of WO$_3$, including construction of hybrid composite structures [12], selective doping of metal and non-metal semiconductors [13], coupling with narrow band-gap semiconductors to form a heterojunction [14] and morphology control such as nanowires, nanoflakes, nanobowls, and nanoparticles [15–17]. Particularly, the combination of WO$_3$ with semiconductors having narrow band-gap has attracted much consideration, including BiVO$_4$ (2.4 eV) [18], CdS (2.4 eV) [19], Fe$_2$O$_3$ [20] (1.97 eV) and Sb$_2$S$_3$ (1.72 eV) [21] because it is an effective approach to promote the separation of the charge carriers. Specifically, Zhang et al. have constructed a WO$_3$/CdS heterojunction achieving a Z-scheme for clean hydrogen fuel evolution by mimicking the natural photosynthesis which can significantly increase the H$_2$ evolution activity of CdS through a Z-scheme mechanism with lactate as electron donor [19]. However most of chalcogenide semiconductors possess the fatal defect of its poor stability under

light illumination. While oxides semiconductors have been promising alternative materials owing to the excellent stability and being environmentally. Cuprous oxide (Cu_2O) is a typical oxide semiconductor which has been widely used in various applications such as photocatalysis [22], Li ion batteries [23], and gas sensors [24]. Since it was demonstrated to be a semiconductor electrode for electrochemical photolysis of water, Cu_2O has been widely investigated as a photocatalyst. There has been growing interest in fabricating ZnO/Cu_2O p-n heterojunction. For example, Guerguerian et al. have prepared ZnO/Cu_2O heterostructure consisted of a ZnO core and a Cu_2O shell and proved that high optical prosperities can be achieved through this heterostructure [25].

Yet, up to date, there are few researches about all oxides semiconductors such as WO_3 NRs coupled with Cu_2O simultaneously to improve photoelectric efficiency in PEC water splitting [26]. We report a facile two-step method to fabricate a novel all oxides heterojunction electrode coupling with WO_3 nanorods and Cu_2O nanoparticles serves as the photoanode. Moreover, different amount of Cu_2O nanoparticles were deposited on the surface of WO_3 nanorods via electrodeposition by adjusting the electrodeposition time. Furthermore, on the basis of optimal amount of Cu_2O nanoparticles, the best photoelectrochemical performance with relatively high photocurrent density of $1.37\,mA\,cm^{-2}$ at $0.8\,V$ vs RHE of WO_3/Cu_2O electrodes were achieved, implying a potential application for PEC water splitting. It is noteworthy that the excellent photocatalytic activity is achieved by virtue of their appropriate energy band gap. Therefore, this present work might broaden a promising concept into PEC water splitting by transforming Cu_2O onto WO_3, resulting in an efficient photoelectrode.

2. Experimental section

2.1. Preparation of WO_3 NRs arrays

The WO_3 nanorods were prepared in two steps as our previous report [21]. Firstly, the WO_3 nanorods arrays were synthesized by a hydrothermal method on the fluorine-doped tin oxide (FTO) glass substrates. Typically, 0.2 g of potassium oxalate monohydrate and 2.4 g of sodium tungstate dihydrate were added in distilled water and then under constant and vigorous stirring for 6 h. In order to control the pH of the precursor solution to 1.0, 2 M concentrated hydrochloric acid was slowly dropped with stirring. Subsequently, the above solution was transferred into a Teflon-lined 100 mL capacity autoclave. After maintained at 180 °C for 24 h, the products were obtained. The obtained samples were washed with distilled water for several times and then dried overnight at 60 °C in air. At last, the WO_3 NRs were achieved after annealing at 550 °C in air for 2 h.

2.2. Fabrication of WO_3 NRs/Cu_2O arrays heterojunction photoelectrodes

The WO_3 NRs/Cu_2O arrays heterojunction were synthesized by electrodeposition process equipped with a three-electrode system which includes Ag/AgCl reference electrode, a metal foil counter electrode and the obtained WO_3 NRs FTO substrate working electrode. The FTO substrate with WO_3 NRs was transferred into the Cu_2O deposition bath containing 0.1 M aqueous solution of copper sulfate ($CuSO_4$) stabilized the Cu^{2+} ions with 3 M lactic acid ($C_3H_6O_3$) as chelating agent. The pH of the solution was adjusted in the range extending from 10 to 12 by adding NaOH. The electrodeposition process was conducted at 50 °C with an applied potential of $-0.4\,V$ vs Ag/AgCl. The amount of Cu_2O depended on the time of electrodeposition ranged from 120 to 360 s. After the electrodeposition process, the substrates were rinsed with distilled water

and absolute ethanol for several times to remove impurity ions remaining in the samples and then naturally dried in air.
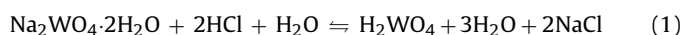
2.3. Characterization

The morphologies and the microstructures of WO_3/Cu_2O NRs arrays were investigated using a JEOL JSM-7800F scanning electron microscope (SEM) and JEOL JEM-2100 transmission electron microscopy (TEM and HRTEM) operated at an accelerating voltage of 100 kV. The crystalline structures of the WO_3/Cu_2O NRs arrays were identified by X-ray diffraction (XRD) (Rigaku-D/max-2500 with Cu Kα radiation) at 40 kV and 200 mA. Optical absorption capabilities of the WO_3/Cu_2O NRs arrays were studied by DU–8 B UV–vis double-beam spectrophotometer. The PEC performance was examined in H_2SO_4 electrolyte (1 mol/L, pH equals to 0) and which was performed via an electrochemical workstation (LK2005A, Tianjin, China), a three-electrode configuration, with WO_3 nanostructures and WO_3/Cu_2O NRs arrays on FTO as the working electrode, saturated Ag/AgCl as reference electrode and a platinum foil as counter electrode, respectively. The potential of Ag/AgCl reported in the results has been converted to the reversible hydrogen electrode (RHE) after electrochemical measurements. The IPCE plots are recorded in the range of 300–800 nm at 0.8 V vs RHE under the AM 1.5G illumination.

3. Results and discussion

3.1. Formation process of WO_3 NRs/Cu_2O arrays

The fabrication process of the WO_3 NRs/Cu_2O arrays is as follows. Prior to hydrothermal reaction, FTO glass substrates were ultrasonically cleaned in a liquid acetone bath and isopropyl alcohol bath of 30 min, respectively. After that, they were dipped into a solution of alcohol for a period of 30 min and rinsed with distilled water. Typically, WO_3 NRs were prepared on the FTO glass substrates in the first-step hydrothermal reaction at a temperature of 180 °C for 24 h. In order to make the samples crystallize completely, there followed by calcinations at 550 °C for 2 h in air. The following chemical reaction could take place during this process:

$$Na_2WO_4 \cdot 2H_2O + 2HCl + H_2O \leftrightharpoons H_2WO_4 + 3H_2O + 2NaCl \qquad (1)$$

$$H_2WO_4 \leftrightharpoons WO_3 + H_2O \qquad (2)$$

Sequentially Cu_2O particles were loaded on the WO_3 NRs arrays by electrodeposition in the solution containing 0.1 M of 0.1 M aqueous solution of copper sulfate ($CuSO_4$) and 3 M lactic acid ($C_3H_6O_3$) which accomplished with a three-electrode system as shown in Fig. 1. The counter electrode was a platinum foil and an Ag/AgCl electrode was used as the reference electrode. Electrodeposition was controlled at $-0.4\,V$ vs Ag/AgCl electrode for different time. When the $CuSO_4$ and $C_3H_6O_3$ were dissolved in distilled water, the solution shows a color of light blue and turns a dark blue when the NaOH was introduced subsequently. In this process, the temperature of the solution was controlled at a constant of 50 °C by means of the motivation and reaction speed is increasing along with the temperature elevated at constant pressure deposition process so that the crystal growth is faster. In order to investigate the influence of different amount of Cu_2O, we prepared the different samples with different deposition time as 120 s, 240 s and 360 s.

In particular, it is noted that in basic solution, formation of Cu_2O is expected according to the following reactions:

$$Cu^{2+} + e^{1-} \rightarrow Cu^{1+} \qquad (3)$$

$$2Cu^{1+} + 2OH^{1-} \rightarrow Cu_2O + H_2O \qquad (4)$$

The morphology and structure of as-obtained materials were characterized by SEM. Fig. 2 shows the SEM images of pristine WO_3
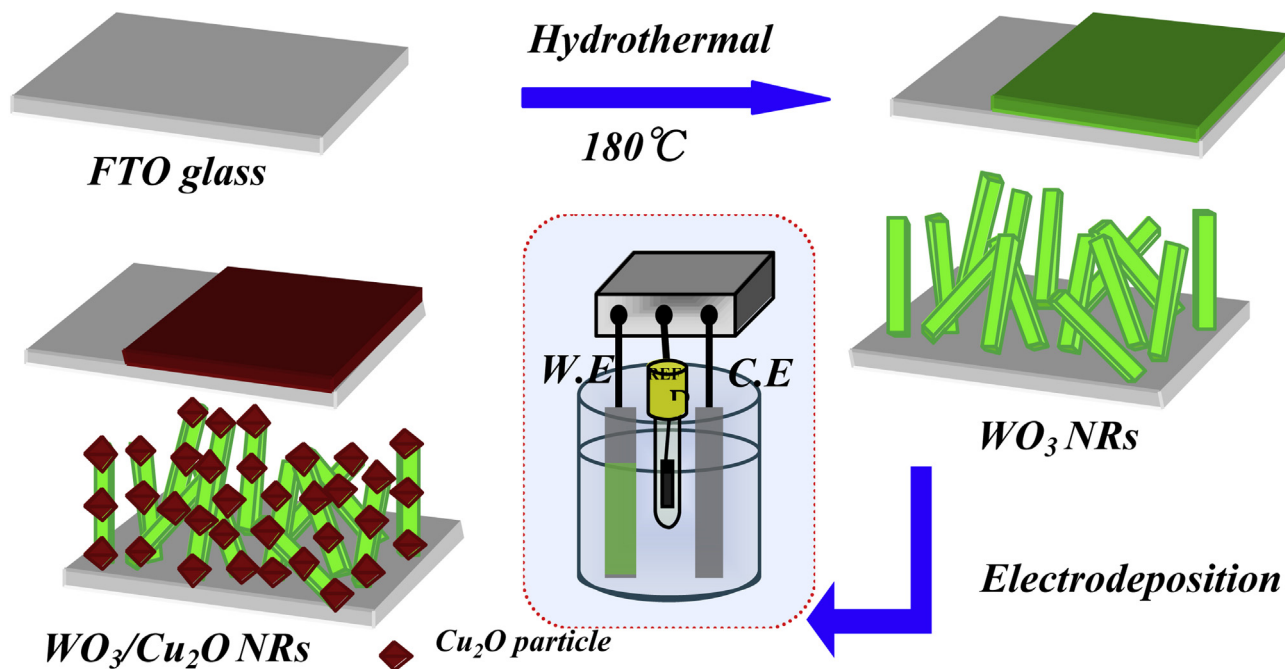
Fig. 1. Schematic representation of synthetic route of WO$_3$ NRs/Cu$_2$O arrays electrodes.
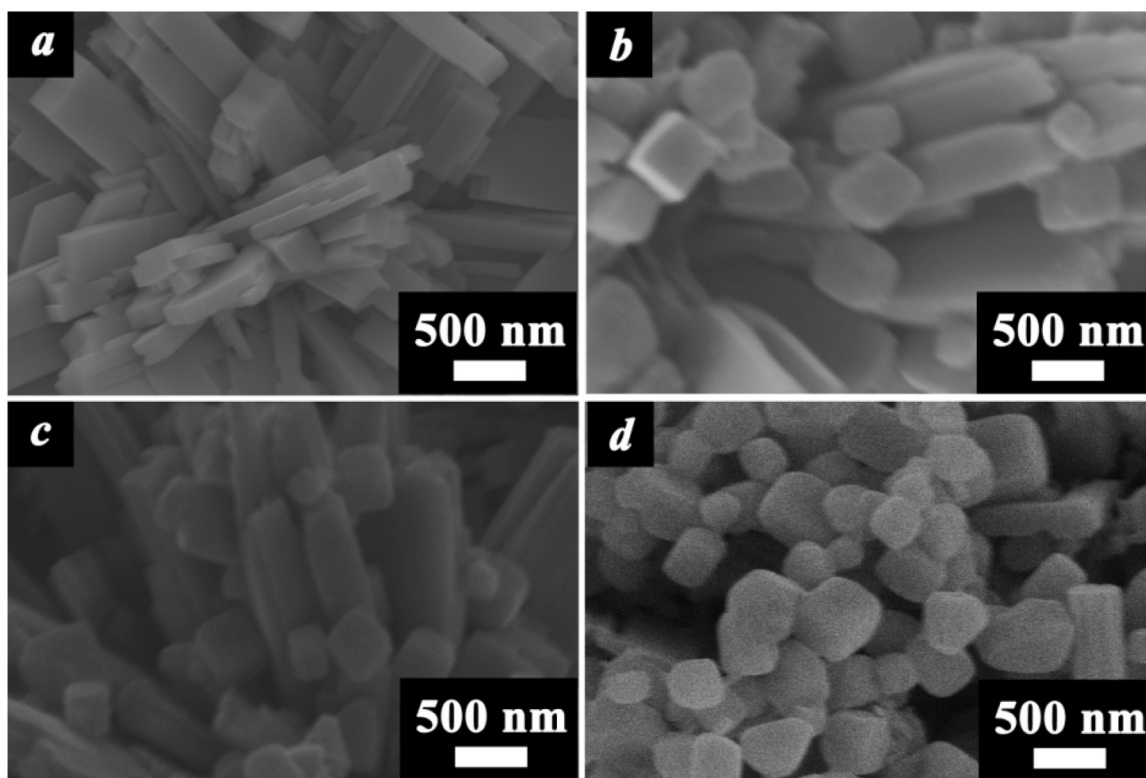

Fig. 2. Typical top view SEM images of pristine WO$_3$ NRs (a) and WO$_3$ NRs/Cu$_2$O arrays for different deposition time: (b) 120 s (c) 240 s (d) 360 s.

NRs (a) and WO$_3$ NRs/Cu$_2$O arrays with different electrodeposition time: samples that deposited in for 120 s, 240 s, 360 s are referred to (b), (c) and (d), respectively. As can be seen from Fig. 2a, the WO$_3$ NRs have monoclinic rod-like morphology grow as aggregation with an average diameter of ~300 nm. In contrast, as shown in Fig. 2b, c and d, the obtained samples inherit the morphology of pre-prepared WO$_3$ NRs as Fig. 2a. Once the Cu$_2$O modification was loaded on the surfaces of WO$_3$ NRs, the top facets of the WO$_3$

NRs became flattened and the side facets demonstrated a rough appearance with vast quantities of minute particles inlaid. This latter observation indexes that the Cu$_2$O nanoparticles were sure deposited onto the surfaces of the WO$_3$ NRs by electrodeposition. To be specific, compared with the morphologies of WO$_3$ NRs/Cu$_2$O arrays of 120 s (Fig. 2b), 240 s (Fig. 2c) and 360 s (Fig. 2d) deposition, the heterojunction structure obtained with 240 s presents an optimal amount of Cu$_2$O nanaoparticles, which would be eventually
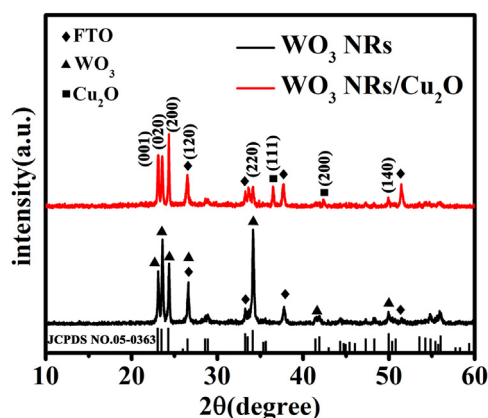
Fig. 3. XRD patterns of the samples.

converted into WO$_3$ NRs/Cu$_2$O arrays structure with an appropriate amount of Cu$_2$O arrays while the former (120 s) is too little and the later (360 s) is too much.

Identification of the phase composition and crystal structure of the as-obtained samples were performed by X-ray diffraction. Fig. 3. shows the XRD patterns of the WO$_3$ NRs and WO$_3$ NRs/Cu$_2$O arrays. It can be seen from the curves that the WO$_3$ nanorods are well indexed as monoclinic phase WO$_3$ (JCPDS Card No. 05-0363) that the standard PDF Card is presented at the bottom of Fig. 3. What can be seen in Fig. 3, with 2θ value around 23.2°, 23.6°, 24.4°, 26.7°, 29.0°, 46.1°, 47.4°, 48.4°, 50.0°, 54.9° and 56.1° could be observed, which can be indexed to the (001), (020), (200), (120), (111), (311), (002), (040), (140), (240) and (420) plane. Moreover, diffraction (111) and (200) with 2θ value around 36.5°and 42.4° can be detected in the XRD pattern of Cu$_2$O indexed by the cubic phase Cu$_2$O (JCPDS Card No. 65-3288) Additionally, the other diffraction peaks are corresponded to the FTO substrate marked with "♦" (JCPDS Card No. 46–1088). The energy dispersive X-ray spectroscopy (EDS) element analysis results (elemental distribution for Cu, O and W shown in Fig. 4) further confirm that the Cu$_2$O are evenly distributed on the surface of the WO$_3$. As we can see, all peaks of Cu, O and W elements are apparently which corresponding to the XRD analysis above.

To verify the component of WO$_3$ NRs/Cu$_2$O arrays furthermore, the selected area elemental mapping spectra of WO$_3$ NRs/Cu$_2$O arrays are investigated. Fig. 5 presents SEM image (a) of WO$_3$ NRs/Cu$_2$O arrays with deposition time of 240 s and the corresponding element distribution mapping. It is obviously can be seen that the Cu (Fig. 5b), O (Fig. 5c), and W (Fig. 5d) elements were distributed onto the FTO substrates, further demonstrated that WO$_3$ NRs were fabricated and massive of Cu$_2$O nanoparticles were successfully deposited on the surface of WO$_3$ NRs.

The detailed microscopic information of Cu$_2$O nanoparticles and the complicated structure of WO$_3$ NRs/Cu$_2$O arrays were observed by TEM, which is vital in understanding how Cu$_2$O nanoparticles were deposited and how the deposition time would eventually affect the morphology of the final products. Fig. 6 shows the TEM images and high magnifications of WO$_3$ NRs/Cu$_2$O arrays deposited with Cu$_2$O for 240 s, respectively. It displays that the bare surface of WO$_3$ NRs appears to be covered by a large amount of smaller particles with an average diameter about 300 nm. What's more, HRTEM characterization shown in Fig. 6c and d also supports the formation of the facets mentioned above. The monoclinic WO$_3$ (200) plane with lattice spacing distance of 0.364 nm and the cubic Cu$_2$O (111) plane with lattice spacing distance of 0.246 nm can be observed clearly, respectively. These experimental results proved that the WO$_3$ NRs/Cu$_2$O arrays were synthesized successfully.

To test the optical properties of the samples, the UV–vis absorption spectra of pristine WO$_3$ NRs (namely 0 s of Cu$_2$O deposition) and different WO$_3$ NRs/Cu$_2$O arrays heterojunction with varying deposition time: 120 s, 240 s, 360 s on FTO substrates are characterized at room temperature which is shown in Fig. 7a. As we can see, the absorption edge of the WO$_3$ NRs is ∼340 nm and with increasing time of electrodeposition, the absorption edge of the WO$_3$ NRs/Cu$_2$O arrays changed from 350 nm to 420 nm. The data was recorded in the wavelength range of 300–800 nm. As expected, along with the Cu$_2$O nanoparticles deposited on WO$_3$ NRs, the optical absorbance was enhanced. It can be clearly seen that WO$_3$ NRs/Cu$_2$O arrays heterojunction shows a wide absorbance and an obvious red shift in the visible region. Such a red shift may be associated with the coupling of WO$_3$ NRs and Cu$_2$O. In contrast, broader absorption region of the WO$_3$ NRs/Cu$_2$O arrays obtained from Cu$_2$O deposition of 240 s were observed with a value at 420 nm, whereas that of the 120 s and 360 s were about 340 nm and 390 nm, respectively. Interestingly, the absorption edge of the WO$_3$ NRs/Cu$_2$O arrays obtained from Cu$_2$O deposition of 360 s is lower than 240 s sample while absorption is increased over wide range of wavelength (450–800 nm). It may arouse by too much Cu$_2$O amount deposited on WO$_3$. It can be concluded that Cu$_2$O nanoparticles could enlarge the photoresponse spectrum to visible region and the photo-absorption of the WO$_3$ NRs/Cu$_2$O arrays heterojunction was enhanced in a certain range, which is related to the narrow energy band as well as the high optical absorption coefficient of Cu$_2$O. Furthermore, the band gap energy of as-prepared WO$_3$ and Cu$_2$O is calculated and the plots of ($\alpha h\nu$) [2] presented in Fig.S1. The band gap energies of WO$_3$ and Cu$_2$O are calculated by 2.9 eV and 2.2 eV, respectively.

The effect of the Cu$_2$O deposited on the WO$_3$ NRs was also explored by the PEC measurement. The PEC measurement was conducted under front illumination (WO$_3$/Cu$_2$O heterojunction structures side illumination). Fig. 7b presents the photocurrent density-voltage (I–V) curves of the WO$_3$ NRs and WO$_3$ NRs/Cu$_2$O arrays heterojunction with different amount of Cu$_2$O. As shown in the photocurrent density-voltage curves, the photocurrent density increased after Cu$_2$O was fabricated on the WO$_3$ NRs and constructing the heterojunction structure. To be specific, the values of photocurrent density of the others were: pure WO$_3$ NRs of 0.39 mA cm^{-2}, WO$_3$ NRs/Cu$_2$O arrays heterojunction with 120 s deposition of 1.01 mA cm^{-2}, WO$_3$ NRs/Cu$_2$O arrays heterojunction with 240 s deposition of 1.37 mA cm^{-2} and WO$_3$ NRs/Cu$_2$O arrays heterojunction with 360 s deposition of 1.21 mA cm^{-2}. The WO$_3$ NRs/Cu$_2$O arrays heterojunction with 240 s deposition again achieved the highest density of photocurrent by 1.37 mA cm^{-2}, which is in agreement with the optical measurement above. Such phenomenon can be concluded that along with the Cu$_2$O was transformed onto the WO$_3$ NRs, the light absorption efficiency was enhanced and the charge transfer was improved. It's worth nothing that an excess of Cu$_2$O amount may arouse lattice scattering and the decreasing of charge carrier concentration [27]. As a result, WO$_3$ NRs/Cu$_2$O arrays heterojunction with 360 s deposition has a decline in photocurrent density which is in agreement with the photo absorbance spectrum (Fig. 7a).

As shown in Fig. 8, the incident photo-to-current conversion efficiency (IPCE) was investigated to further explore the connection between light absorption and the density of photocurrent. It is obviously seen that the WO$_3$ NRs/Cu$_2$O arrays heterojunction photoelectrodes presented a photoactivity enhancement compared to the pure WO$_3$ NRs under visible light, which is in accordance with the I–V curves presented in Fig. 7b. The energy conversion efficiency value of WO$_3$ NRs/Cu$_2$O arrays heterojunction photoelectrode exhibited by 10.7% which corresponds to a maximum photocurrent density of 1.37 mA cm^{-2}. The enhanced IPCE of WO$_3$ NRs/Cu$_2$O arrays heterojunction photoelectrodes contributes to
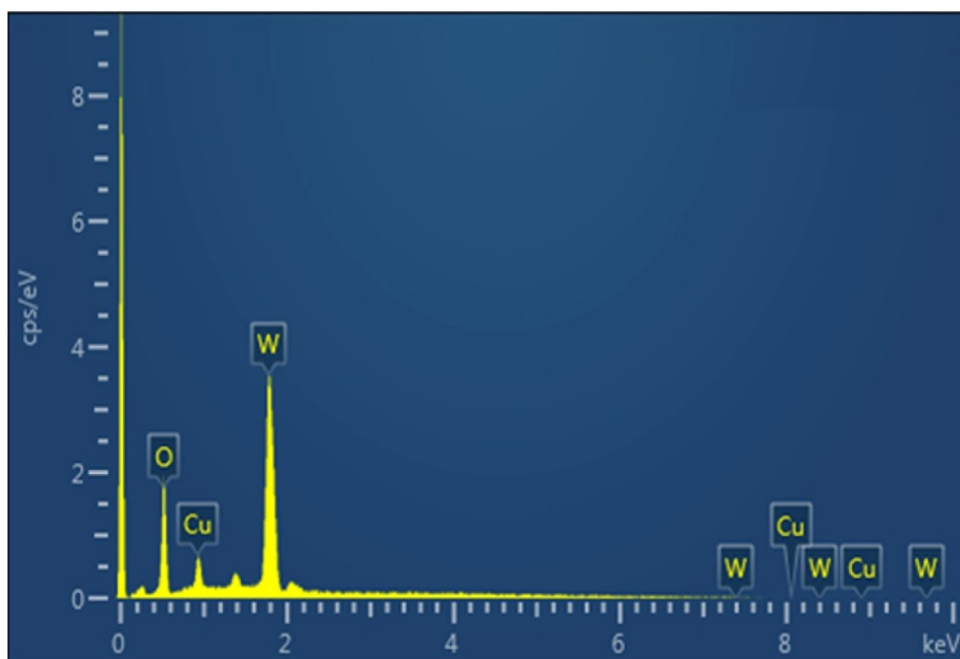
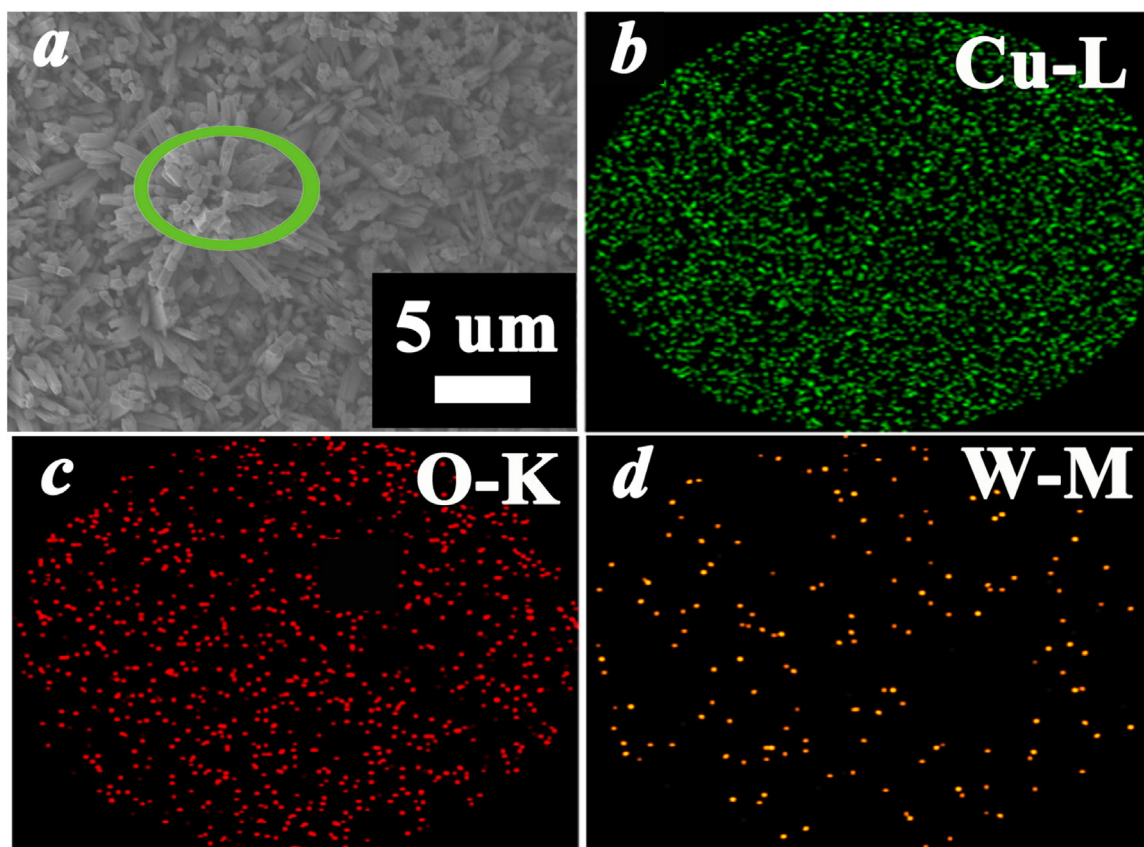**Fig. 4.** EDS elemental analysis of the samples.

Fig. 5. SEM image (a) of WO$_3$ NRs/Cu$_2$O arrays with deposition time of 240 s and the corresponding element distribution mapping of Cu (b), O (c)and W (d).

significant amelioration of photoelectrocatalytic effect by Cu$_2$O deposited on the WO$_3$ NRs within a certain range.

Hence we were motivated to explore the electrochemical interfacial properties of the different samples, the electrochemical impedance spectroscopy (EIS) was investigated. Fig. 9 shows the

EIS Nyquist plots of pure WO$_3$ NRs and the WO$_3$ NRs/Cu$_2$O arrays heterojunction with different deposition time ranged from 120 s to 360 s at 0.8 V vs RHE, respectively. Specifically, a reduced amount of photogenerated electrons recombine with photogenerated holes which leads to a higher concentration of charge carriers and dis-
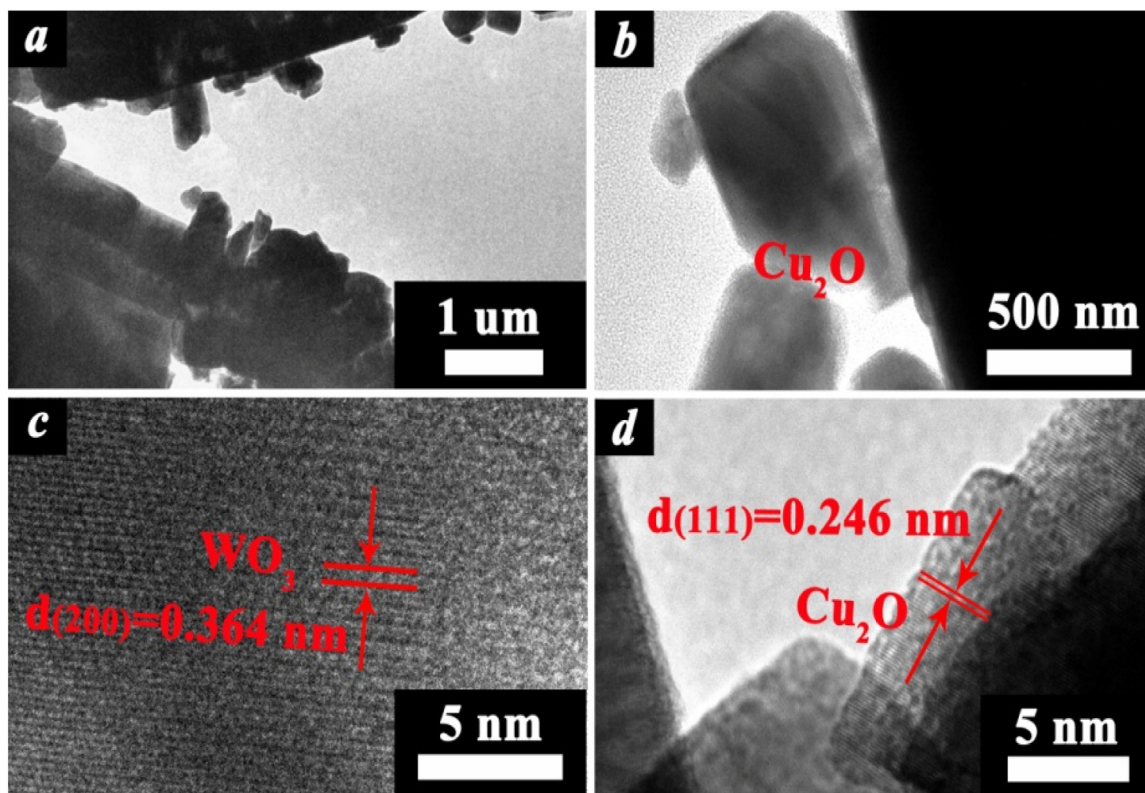
Fig. 6. TEM images of WO$_3$ NRs/Cu$_2$O arrays (a), Cu$_2$O particles (b) and HRTEM images of WO$_3$ NRs (c), Cu$_2$O particles (d).
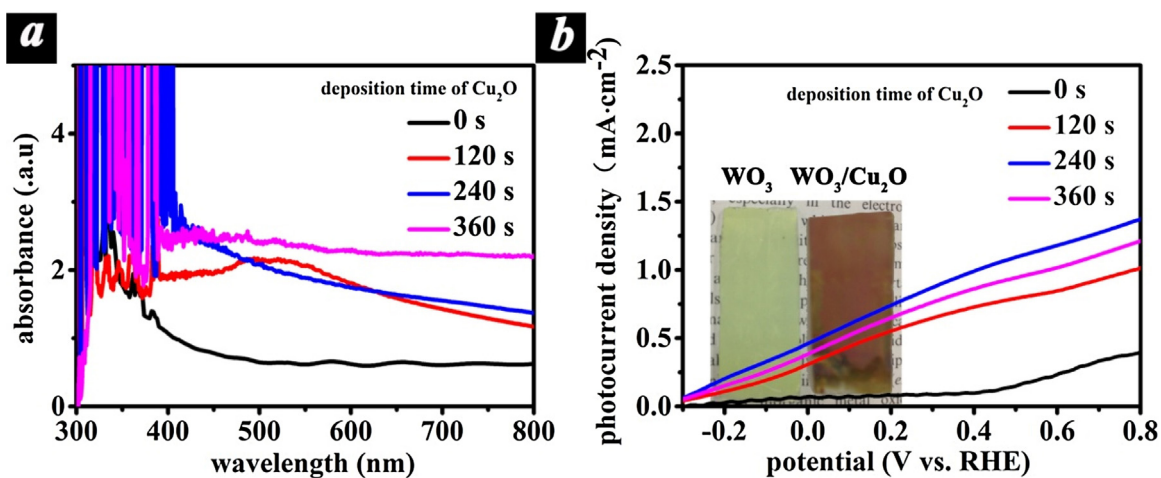

Fig. 7. UV–vis absorbance spectra (a) and the Photocurrent density-voltage curves (b) of the samples.

played smaller arc radius. On the other hand, more photogenerated electrons were calculated in the interface of the samples, more photogenerated holes would be consumed in electron-hole recombination which presented with a bigger arc radius. Based on the above mechanism, WO$_3$ NRs/Cu$_2$O arrays heterojunction possessed fast electron-hole transfer speed and reduced recombination rate owing to the appropriate band-gap structure instituted compared to the pure WO$_3$ NRs.

In order to investigate the origins of these excellent photo-electrocatalytic properties, a study of the interaction between the WO$_3$ NRs/Cu$_2$O arrays heterojunction photocatalyst and band gap structure is essential. Fig. 10 presents the schematic of the WO$_3$ NRs/Cu$_2$O arrays heterojunction photoanode applied in overall water splitting. In this kind of heterojunction composite struc-

ture, WO$_3$ and Cu$_2$O will be excited by the light illumination to generate the electron-hole pairs contributes to a consequence of improved light absorbance. Moreover, the photogenerated electrons will transfer from the conduction band (−0.28 eV) of Cu$_2$O to that of WO$_3$ (0.64 eV) and the photogenerated holes will transfer from the valence band (3.54 eV) of WO$_3$ to that of Cu$_2$O (1.92 eV). As shown in the simplified schematic illustration of the band-gap energy diagram of WO$_3$ NRs/Cu$_2$O arrays heterojunction photoanode, this appropriate gradient energy band-gap mechanism can facilitate the separation of the electron-hole pairs and improve the efficient in the photocurrent conversion process. This improvement in performance was found to be in optical measurements of the improved light absorption spectrum and photocurrent surveys.
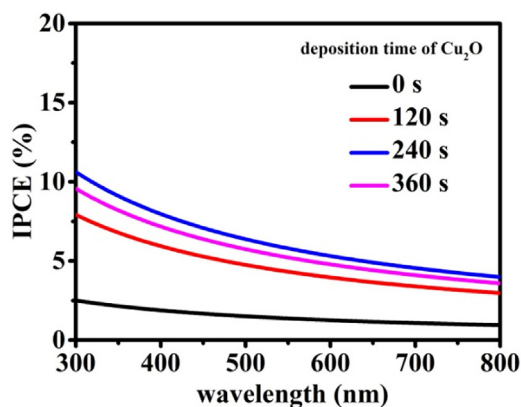
Fig. 8. Incident Photon-to-current Conversion Efficiency (IPCE) plots in the range of 300–800 nm at 0.8 V vs RHE of the samples.
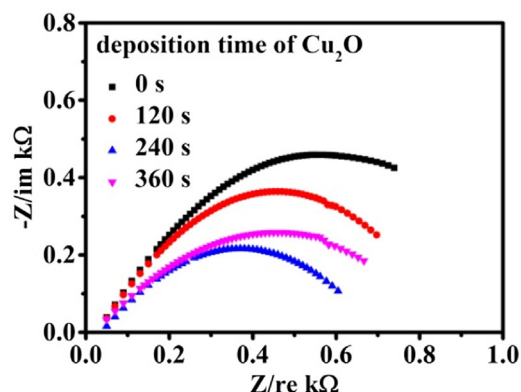

Fig. 9. Electrochemical impedance spectroscopy of the samples.
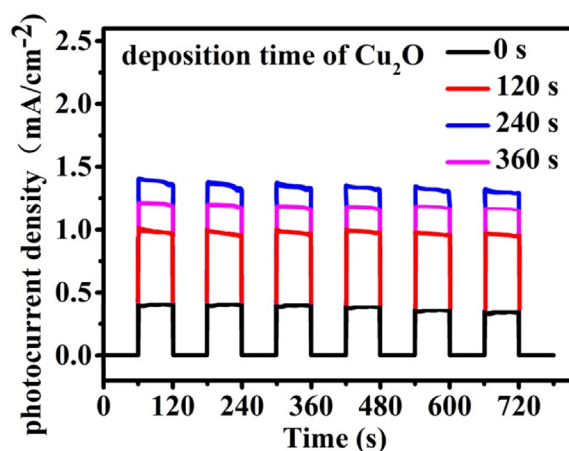

Fig. 11. Transient photocurrent response of the samples at 0.8 V vs RHE with a 60 s light on/off.

pared with the other photoelectrodes. In addition, as presented in Fig. 11, the transient photocurrent curves all show a quick response once the light turned on because of electrons in WO_3/Cu_2O heterojunction structures gathered before the light switched while back to zero when the light is off which indicates the as-obtained samples response sensitively to the light illumination. Moreover, there is a specific decay during the illumination period because of the photogenerated charge carriers accumulated before the light turned on. In practical terms, the photogenerated charge carriers were concentrated during the continued light illumination [28].

5. Conclusions

High efficient all oxides semiconductor WO_3 NRs/Cu_2O arrays heterojunction was fabricated via hydrothermal and electrodeposition used as photoelectrode for PEC water splitting. The increased optical and photoelectrochemial properties of the WO_3 NRs/Cu_2O arrays heterojunction have been investigated. The Cu_2O deposited for 240 s on WO_3 NRs FTO substrate shows an enhancement in photoelectrochemial capability and presented the highest photocurrent of 1.37 mA cm^{-2} at 0.8 V vs RHE. The enhancement in photocurrent density is not only due to the broader optical absorption spectrum but also to the better photogenerated charge separation efficiency, as evidenced respectively from UV–vis spectroscopy and EIS measurement. The electrodeposition of Cu_2O onto WO_3 NRs constructed a heterojunction structure, which increases the ability of light absorption and suppresses the recombination of photogenerated electron-hole based on the appropriate gradi-
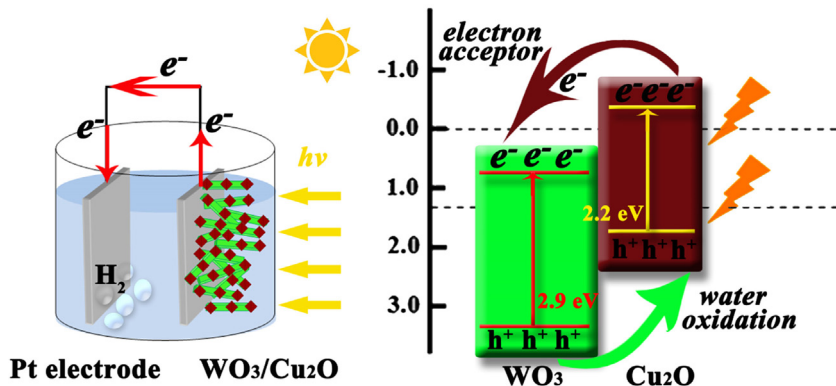
Through measurement of the optical and photoelectrochemical prosperities of the as-obtained samples, the feasibility of WO_3 NRs/Cu_2O arrays heterojunction photoelectrodes used in PEC water splitting has been assessed. To further support the assumption that Cu_2O as an oxide semiconductor showing better corrosion resistance to light, the stability of the photoelectrodes under illumination is has been evaluated by transient photocurrent response at 0.8 V vs RHE over 700 s. The stability of WO_3 NRs/Cu_2O arrays heterojunction photoelectrodes is measured by the percentage of the photocurrent density at the end of the last light cycle compared to that at the beginning of the first cycle within the 720 s measurement period. WO_3 NRs/Cu_2O arrays heterojunction photoelectrode with 240 s deposition shows a slightly decreased in photocurrent com-

Fig. 10. Schematic of the WO_3 NRs/Cu_2O arrays heterojunction photoanode applied in overall water splitting and simplified schematic illustration of the band-gap energy diagram, showing the enhanced light-harvesting and charge-transfer processes.

ent band-gap structure. This promising all oxides semiconductor heterojuction structure suggests a new sight applied in solar-to-hydrogen conversion devices.

Acknowledgements

Appendix A. Supplementary data

Supplementary data associated with this article can be found, in the online version, at http://dx.doi.org/10.1016/j.apcatb.2016.08.025.

References

[1] E.L. Miller, Photoelectrochemical water splitting, Energy Environ. Sci. 8 (2015) 2799–3050.
[2] T. Hisatomi, J. Kubota, K. Domen, Recent advances in semiconductors for photocatalytic and photoelectrochemical water splitting, Chem. Soc. Rev. 43 (2014) 7520–7535.
[3] A. Fujishima, K. Honda, Electrochemical photolysis of water at a semiconductor electrode, Nature 238 (1972) 37–38.
[4] G.M. Wang, H.Y. Wang, Y.C. Ling, Y.C. Tang, X.Y. Yang, R.C. Fitzmorris, C.C. Wang, J.Z. Zhang, Y. Li, Hydrogen-treated TiO_2 nanowire arrays for photoelectrochemical water splitting, Nano Lett. 11 (2011) 3026–3033.
[5] M.F. Shao, F.Y. Ning, M. Wei, D.G. Evans, X. Duan, Hierarchical nanowire arrays based on ZnO core- layered double hydroxide shell for largely enhanced photoelectrochemical water splitting, Adv. Funct. Mater. 24 (2014) 580–586.
[6] K. Sivula, F. Le Formal, M. Grätzel, Solar water splitting: progress using hematite (α-Fe_2O_3) photoelectrodes, ChemSusChem 4 (2011) 432–449.
[7] Y.H. Ng, A. Iwase, A. Kudo, R. Amal, Reducing graphene oxide on a visible-light $BiVO_4$ photocatalyst for an enhanced photoelectrochemical water splitting, J. Phys. Chem. Lett. 1 (2010) 2607–2612.
[8] P. Dias, T. Lopes, L. Meda, L. Andrade, A. Mendes, Photoelectrochemical water splitting using WO_3 photoanodes: the substrate and temperature roles, Phys. Chem. Chem. Phys. 18 (2016) 5232–5243.
[9] V. Cristino, S. Caramori, R. Argazzi, L. Meda, G.L. Marra, C.A. Bignozzi, Efficient photoelectrochemical water splitting by anodically grown WO_3 electrodes, Langmuir 27 (2011) 7276–7284.
[10] J.Y. Zheng, Z. Haider, T.K. Van, A.U. Pawar, M.J. Kang, C.W. Kim, Y.S. Kang, Tuning of the crystal engineering and photoelectrochemical properties of crystalline tungsten oxide for optoelectronic device applications, CrystEngComm 17 (2015) 6070–6093.
[11] N. Wang, D.E. Wang, M.R. Li, J.Y. Shi, C. Li, Photoelectrochemical water oxidation on photoanodes fabricated with hexagonal nanoflower and nanoblock WO_3, Nanoscale 6 (2014) 2061–2066.
[12] H.J. Li, Y. Zhou, L. Chen, W.J. Luo, Q.F. Xu, X.Y. Wang, M. Xiao, Z.G. Zou, Rational and scalable fabrication of high-quality WO_3/CdS core/shell nanowire arrays for photoanodes toward enhanced charge separation and transport under visible light, Nanoscale 5 (2013) 11933–11939.
[13] M. Horprathum, T. Srichaiyaperk, B. Samransuksamer, A. Wisitsoraat, P. Eiamchai, S. Limwichean, C. Chananonnawathorn, K. Aiempanakit, N. Nuntawong, V. Patthanasettakul, C. Oros, S. Porntheerapht, P. Songsiriritthigul, H. Nakajima, A. Tuantranont, P. Chindaudom, Ultrasensitive hydrogen sensor based on Pt-decorated WO_3 nanorods prepared by glancing-angle dc magnetron sputtering, ACS Appl. Mater. Interfaces 6 (2014) 22051–22060.
[14] K.M. Nam, E.A. Cheon, W.J. Shin, A.J. Bard, Improved photoelectrochemical water oxidation by the WO_3/$CuWO_4$ composite with a manganese phosphate electrocatalyst, Langmuir 31 (2015) 10897–10903.
[15] M.S. Yao, Q.H. Li, G.L. Hou, C. Lu, B.L. Cheng, K.C. Wu, G. Xu, F.L. Yuan, F. Ding, Y.F. Chen, Dopant-controlled morphology evolution of WO_3 polyhedra synthesized by RF thermal plasma and their sensing properties, ACS Appl. Mater. Interfaces 7 (2015) 2856–2866.
[16] R.H. Gonçalves, L.D. Leite, E.R. Leite, Colloidal WO_3 nanowires as a versatile route to prepare a photoanode for solar water splitting, ChemSusChem 5 (2012) 2341–2347.
[17] W.J. Li, P.M. Da, Y.Y. Zhang, Y.C. Wang, X. Lin, X.G. Gong, G.F. Zheng, WO_3 nanoflakes for enhanced photoelectrochemical conversion, ACS Nano 8 (2014) 11770–11777.
[18] P.M. Rao, L.L. Cai, C. Liu, I.S. Cho, C.H. Lee, J.M. Weisse, P.D. Yang, X.L. Zheng, Simultaneously efficient light absorption and charge separation in WO_3/$BiVO_4$ core/shell nanowire photoanode for photoelectrochemical water oxidation, Nano Lett. 14 (2014) 1099–1105.
[19] L.J. Zhang, S. Li, B.K. Liu, D.J. Wang, T.F. Xie, Highly efficient CdS/WO_3 photocatalysts: Z-scheme photocatalytic mechanism for their enhanced photocatalytic H_2 evolution under visible light, Am. Chem. Soc. Catal. 4 (2014) 3724–3729.
[20] K. Sivula, F.L. Formal, M. Grätzel, WO_3-Fe_2O_3 photoanodes for water splitting: a host scaffold, guest absorber approach, Chem. Mater. 21 (2009) 2862–2867.
[21] J. Zhang, Z.H. Liu, Z.F. Liu, Novel WO_3/Sb_2S_3 heterojunction photocatalyst based on WO_3 of different morphologies for enhanced efficiency in photoelectrochemical water splitting, ACS Appl. Mater. Interfaces 8 (2016) 9684–9691.
[22] J.S. Luo, L. Steier, M.K. Son, M. Schreier, M.T. Mayer, M. Grätzel, Cu_2O nanowire photocathodes for efficient and durable solar water splitting, Nano Lett. 16 (2016) 1848–1857.
[23] Y.H. Lee, I.C. Leu, C.L. Liao, S.T. Chang, M.T. Wu, J.H. Yen, K.Z. Fung, Fabrication and characterization of Cu_2O nanorod arrays and their electrochemical performance in Li-ion batteries, Electrochem. Solid State Lett. 9 (2006) A207–A210.
[24] S. Deng, V. Tjoa, H.M. Fan, H.R. Tan, D.C. Sayle, M. Olivo, S. Mhaisalkar, J. Wei, C.H. Sow, Reduced graphene oxide conjugated Cu_2O nanowire mesocrystals for high-performance NO_2 gas sensor, J. Am. Chem. Soc. 134 (2012) 4905–4917.
[25] G. Guerguerian, F. Elhordoy, C.J. Pereyra, R.E. Marotti, F. Martín, D. Leinen, J. Ramos-Barrado, E.A. Dalchiele, ZnO/Cu_2O heterostructure nanopillar arrays: synthesis, structural and optical properties, J. Phys. D: Appl. Phys. 45 (2012) 245301.
[26] L.J. Minggu, K.H. Ng, H.A. Kadir, M.B. Kassim, Bilayer n-WO_3/p-Cu_2O photoelectrode with photocurrent enhancement in aqueous electrolyte photoelectrochemical reaction, Ceramics Int. 40 (2014) 16015–16021.
[27] N. Helaili, Y. Bessekhouad, A. Bouguelia, M. Trari, P-Cu_2O/n-ZnO heterojunction applied to visible light orange II degradation, Sol. Energy 84 (2010) 1187–1192.
[28] S.G. Kumar, L.G. Devi, Review on modified TiO_2 photocatalysis under UV/visible light: selected results and related mechanisms on interfacial charge carrier transfer dynamics, J. Phys. Chem. A 115 (2011) 13211–13241.